

Highly efficient anion exchange membrane water electrolyzers via chromium-doped amorphous electrocatalysts

Received: 9 January 2024

Accepted: 8 April 2024

Published online: 22 April 2024

Check for updates

Sicheng Li^{1,5}, Tong Liu^{1,5}, Wei Zhang¹✉, Mingzhen Wang², Huijuan Zhang¹, Chunlan Qin¹, Lingling Zhang¹, Yudan Chen¹, Shuaiwei Jiang¹, Dong Liu¹, Xiaokang Liu¹, Huijuan Wang³, Qiquan Luo⁴, Tao Ding¹✉ & Tao Yao¹✉

In-depth comprehension and modulation of the electronic structure of the active metal sites is crucial to enhance their intrinsic activity of electrocatalytic oxygen evolution reaction (OER) toward anion exchange membrane water electrolyzers (AEMWEs). Here, we elaborate a series of amorphous metal oxide catalysts (FeCrO_x , CoCrO_x and NiCrO_x) with high performance AEMWEs by high-valent chromium dopant. We discover that the positive effect of the transition from low to high valence of the Co site on the adsorption energy of the intermediate and the lower oxidation barrier is the key factor for its increased activity by synchrotron radiation in-situ techniques. Particularly, the CoCrO_x anode catalyst achieves the high current density of 1.5 A cm^{-2} at 2.1 V and maintains for over 120 h with attenuation less than 4.9 mV h^{-1} in AEMWE testing. Such exceptional performance demonstrates a promising prospect for industrial application and providing general guidelines for the design of high-efficiency AEMWEs systems.

Anion exchange membrane (AEM) electrolysis is considered a pivotal technology for the sustainable energy economy^{1,2}. It has advantages over proton exchange membrane (PEM) technology with noble metal oxide (IrO_2) anodes. These advantages include the ability to use less expensive non-platinum group metal (PGM) catalysts on the anode side, cheaper ion exchange membranes, free of environmentally harmful fluorine-based polymers, and no need for acid-resistant stacking materials, resulting in lower overall device costs^{3–6}. Nevertheless, AEMWE technology is a relatively new technology and faces many issues that have to be solved before fulfilling its full potential, with catalysts being a crucial factor⁷. There are two major challenges in developing higher performance non-noble metal anode OER electrocatalysts. One is that current synthesis methods for these catalysts are not optimized for industrial applications. Therefore, in practical scenarios, it is essential to consider simple and easily accessible synthesis

methods that can produce large quantities of catalysts. The other is that although Ni/Fe-based materials have been extensively studied as OER catalysts, their stability is poor and they are rarely used in AEM electrolysis research⁸. The stability and activity are both critical factors especially in the electrolysis applications, which should receive more attention.

On the anode side of AEMWEs, the OER is a complex process involving the transfer of multiple electrons. As the electrons are transferred, the valence state of the active metal changes, which is believed to be the source of the OER intrinsic activity⁹. Hence, there is ongoing debate regarding the relationship between the valence state and activity of the active site in transition-metal-based catalysts (Fig. 1a). Numerous studies have revealed that transition metal compounds with high oxidation state metal sites exhibit great OER activity, while those with low oxidation metal sites have comparatively low

¹School of Nuclear Science and Technology, Key Laboratory of Precision and Intelligent Chemistry, Hefei National Research Center for Physical Sciences at the Microscale, National Synchrotron Radiation Laboratory, University of Science and Technology of China, Hefei, P.R. China. ²Zhongke Enthalpy (Anhui) New Energy Technology Co. Ltd, Hefei, P.R. China. ³Experimental Center of Engineering and Materials Science, University of Science and Technology of China, Hefei, P.R. China. ⁴Institutes of Physical Science and Information Technology, Anhui University, Hefei, P.R. China. ⁵These authors contributed equally: Sicheng Li, Tong Liu. ✉e-mail: zhangw94@ustc.edu.cn; dingtao@ustc.edu.cn; yaot@ustc.edu.cn

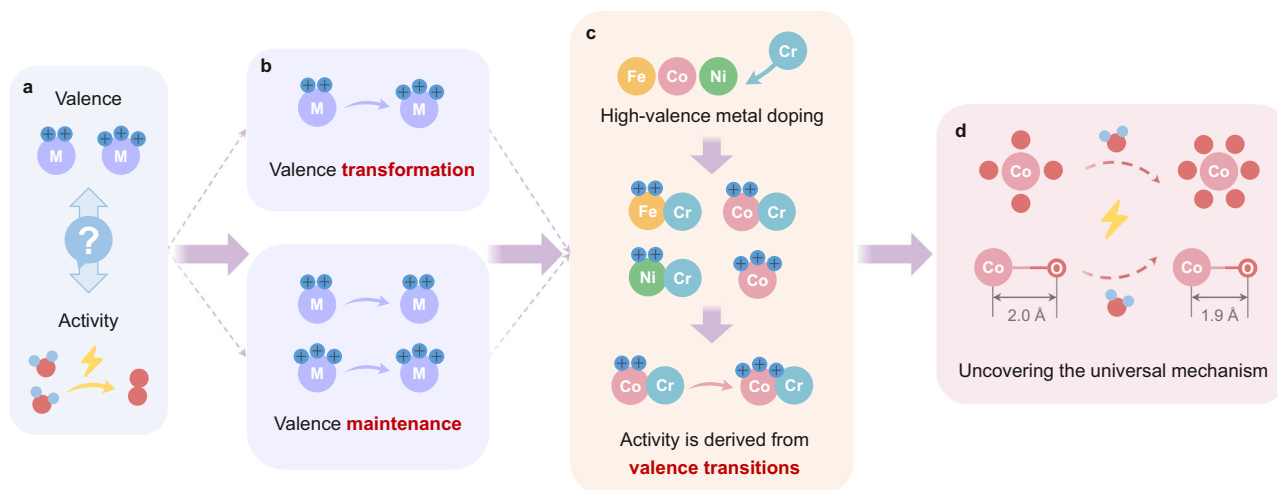


Fig. 1 | Schematic diagram of the origin of the research and design ideas. **a** The inherent debate between active site valence and catalytic activity. **b** Different types of valence changes during the OER. **c** A series of meticulously conceived and

designed experiments were conducted using Cr as the high-valence dopant. **d** Uncovering valence changes and universal mechanisms impacting catalytic performance.

activity^{10,11}. However, recent research has challenged this notion, suggesting that low oxidation metal sites can also play a significant role in determine OER activity^{12–14}. Based on this theory, scientists have introduced oxygen-rich defects¹⁵ and doped high valence metals (such as W¹⁶, Mo¹⁷, Nb¹³ and Cr¹⁸) to lower the valence state of the active metal. Despite these efforts, the relationship between catalytic activity and valence changes during the reaction remains unclear, owing to the lack of the dynamic evolution analysis of active metal sites during the OER condition (Fig. 1b). In-depth understanding and regulation of the electronic structure of the active metal sites in catalysts, as well as their application in practical AEMWEs for mechanistic comprehension, remains a significant challenge. Synchrotron radiation in-situ techniques provide a practical way to address this issue by monitoring the dynamics of the valence state and elucidating the key reasons for its impact on catalytic performance.

In this work, we chose low-cost, abundant Cr with high valence charge as the metal dopant and utilized a one-step liquid phase reduction method to synthesize a series of efficient amorphous metal oxide catalysts for AEMWEs (Fig. 1c). Among them, the CoCrO_x catalyst delivered outstanding activity and stability. We used in-situ valence to core X-ray emission spectroscopy (vtc-XES) for the first time in the electrocatalytic system to precisely identify the ligands of Co, and the σ -interaction strength enhancement of Co-O during the OER process. The combination of in-situ X-ray absorption spectroscopy (XAS), synchrotron radiation infrared (SR-IR) and other experiments along with theoretical calculations allowed us to discern the atomic and electronic structure evolution at the Co site optimizes the adsorption energy of the oxygen intermediate (Fig. 1d), resulting in the low oxidation energy barrier that are crucial for high catalytic activity. Impressively, the AEMWE was assembled by using CoCrO_x as anode catalyst achieved the high current density of 1.5 A cm⁻² at 2.1 V and exhibited outstanding long-term durability for operating over 120 h at 0.5 A cm⁻², further demonstrating its great potential in the application of water electrolysis industry.

Results

Synthesis and structural characterization

A diagram of the catalysts synthetic method is shown in Fig. 2a. The catalysts were prepared by a simple one-step liquid-phase reduction method by mixing NaBH₄ with the solution of different metal chlorides under stirring, following by washing and drying at room temperature. The presence of NaBH₄ facilitated the simultaneous reduction of the metal precursors during the nucleation and growth phases.

This reduction process also allowed for the instantaneous formation of three-dimensional networks through the fusion of metal nuclei¹⁹, enabling the facile preparation of high performance catalysts. The morphology of the prepared catalysts was observed using the scanning electron microscopy (SEM), revealing the porous characteristics of FeCrO_x, CoCrO_x and NiCrO_x (Fig. 2b and Supplementary Fig. 1). Moreover, the structural features were investigated by transmission electron microscopy (TEM), which indicated that the prepared catalysts as the disordered atomic structure (Fig. 2c), and spherical nanoparticles with an average size of about 20 nm were observed (Fig. 2d). The high-resolution TEM (HRTEM) and aberration-corrected high-angle annular dark-field scanning transmission electron microscopy (AC HAADF-STEM) further showed that there were no obvious lattice striations (Fig. 2e and Supplementary Fig. 2), indicating its amorphous nature. X-ray diffraction (XRD) pattern (Supplementary Fig. 3) showed very broad and weak diffraction peaks, indicating the long-range disorder feature. The amorphous character is further confirmed by the diffraction rings shown by selected area electron diffraction (SAED) (Fig. 2f)^{20,21}, with the bright inner rings suggesting the short-range order feature²². The morphology and structure of FeCrO_x and NiCrO_x were found to be similar to CoCrO_x (Supplementary Figs. 4–7). In addition, energy-dispersive X-ray spectroscopy (EDS) mapping analysis showed that Co, Cr, and O were uniformly distributed throughout the architecture (Fig. 2g), demonstrating the formation of CoCr oxides rather than phase-separated mixed structures. The same phenomenon was observed for FeCrO_x and NiCrO_x (Supplementary Fig. 8), while the higher O content is attributed to the ease of oxidation of the transition metals. The inductively coupled plasma-atomic emission spectrometer (ICP-AES) was used to further determine the elemental ratios of the prepared catalysts (Supplementary Table 1). The results showed that the atomic ratios of Fe, Co, Ni to Cr were close to 1:1, indicating the precise control of the synthetic method adopted in this study. Furthermore, the extended X-ray absorption fine structure (EXAFS) spectra was used to confirm that the CoCrO_x, FeCrO_x and NiCrO_x (Fig. 2h, i and Supplementary Figs. 9–12) catalysts had similar local structures and coordination environments, suggesting that each form structurally similar MCr (M=Fe, Co and Ni) oxides, which lays the basis for further analysis.

Electrocatalytic OER and AEMWEs performance

The OER activity measurements of the catalysts were conducted in O₂-saturated 1M KOH solution by using a standard three-electrode system. The optimal catalytic performance of the samples was

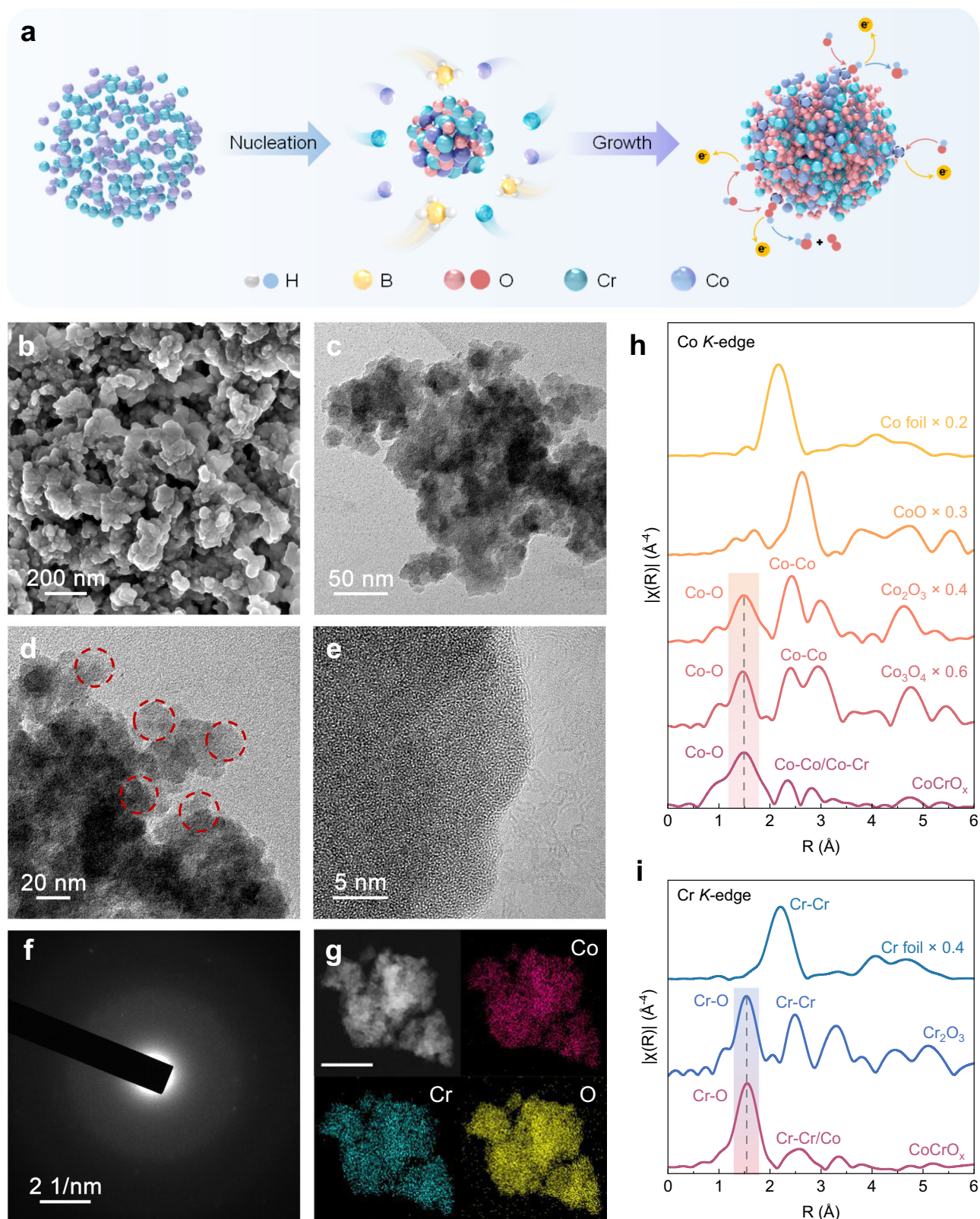


Fig. 2 | Preparation, structural and morphological characteristics of CoCrO_x. **a** Illustration of the preparation procedure, **(b)** SEM, **(c, d)** TEM, **(e)** HRTEM images, **f** SAED patterns, **g** EDS mappings showing the dispersion of Co (pink), Cr (blue-

green) and O (yellow), respectively. Scale bar: 100 nm. EXAFS spectra of **(h)** Co K-edge and **(i)** Cr K-edge for CoCrO_x and reference samples.

achieved when the atomic ratio of Co/Cr was 1:1, as determined through performance-based screening (Supplementary Fig. 13). For the sake of clarity, the atomic ratio of Fe/Co/Ni to Cr for the FeCrO_x, CoCrO_x and NiCrO_x catalysts is 1:1 unless otherwise specified. To assess

the impact of Cr doping, we synthesized a non-Cr doped CoO_x catalyst and also included the benchmark RuO₂ catalyst for comparison. As shown in the iR-corrected LSV curves (Fig. 3a), the CoCrO_x exhibited superior OER performance, necessitating a mere overpotential of

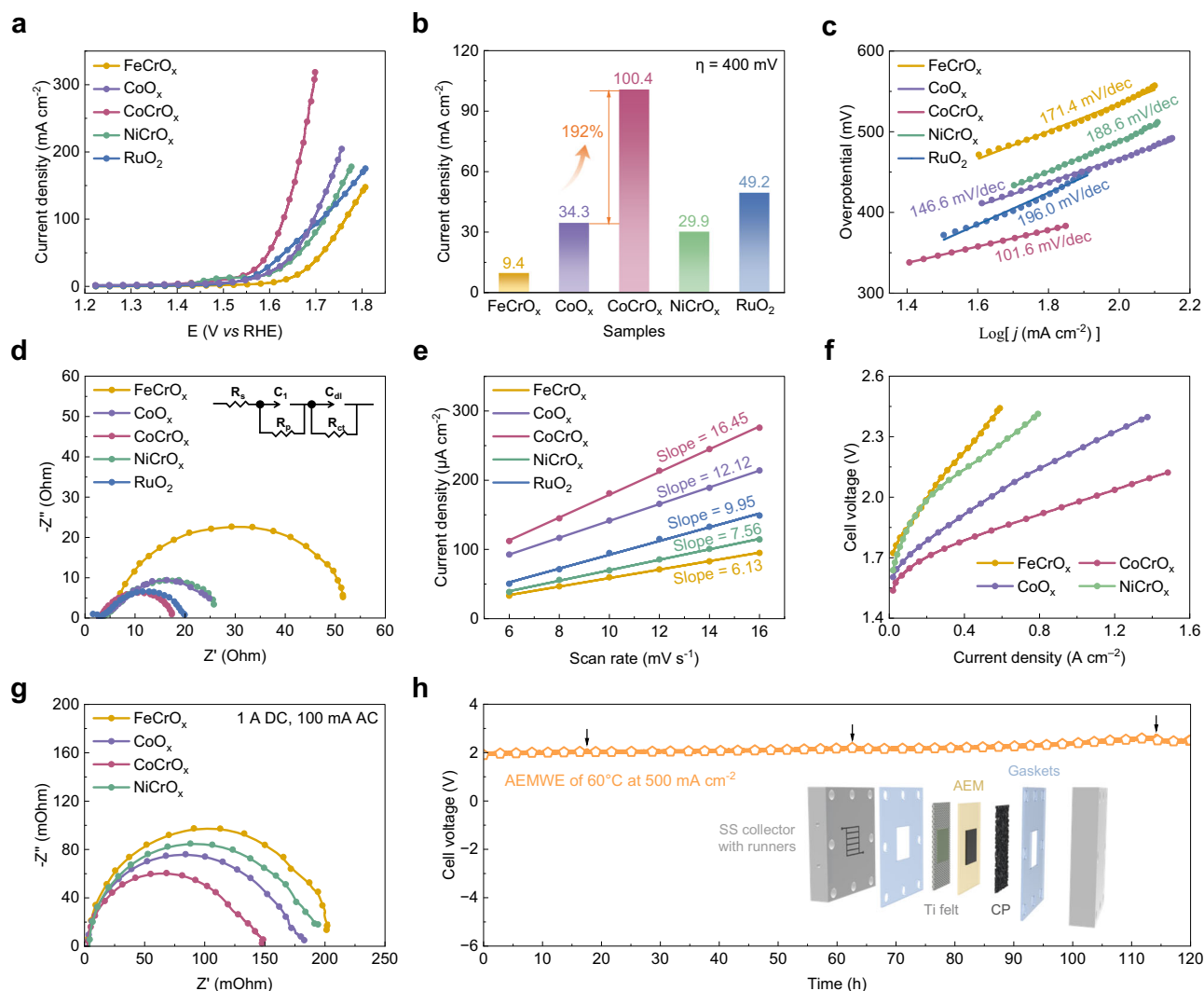


Fig. 3 | Electrochemical activity and stability. **a** LSV curves of FeCrO_x, CoCrO_x, NiCrO_x, CoO_x and RuO₂ catalysts in 1M KOH at the scan rate of 5 mV s⁻¹. **b** The current density of different catalysts recorded at 400 mV. **c** Tafel plots. **d** Nyquist plots acquired at 1.57 V (*vs* RHE) in half cell. Inserts in panels d show equivalent circuit of the OER. **e** Differences in current densities plotted against scan rates to

determine the ECSA. **f** I–V curves of AEMWEs the prepared catalysts as anodes. **g** Nyquist plots of AEMWEs applying 1 A direct current (DC) and 100 mA root mean square (RMS) of alternating current (AC). **h** Chronopotentiometry curve of CoCrO_x catalyst at constant current density of 0.5 A cm⁻² in the AEMWEs at 60 °C. Positions indicated by the black arrows represent that the replacement of electrolyte.

268 mV to achieve the current density of 10 mA cm⁻². The performance outmatched that of other prepared catalysts and the comparative CoO_x catalyst (323 mV), surpassing even the commercial RuO₂ (314 mV). It suggested that the beneficial impact of Cr doping on enhancing the OER activity. As the overpotential was fixed at 400 mV, the current density of CoCrO_x considerably exceeded other catalysts, being 10.7 times, 3.4 times, and twice as high as FeCrO_x, NiCrO_x, and RuO₂, respectively. Significantly, Cr doping also enhanced the current density by 192% relative to CoO_x (Fig. 3b). Additionally, in order to further investigate the intrinsic activity of the catalysts, the Tafel slope was further obtained from the corresponding LSV curves (Fig. 3c). With a Tafel slope of 101.6 mV dec⁻¹, the CoCrO_x significantly outperformed other catalysts, including the non-Cr doped CoO_x catalyst (146.6 mV dec⁻¹) and RuO₂ (196.0 mV dec⁻¹), indicative of the more favorable OER kinetics. The electrochemical impedance spectra (EIS) (Fig. 3d) revealed that CoCrO_x exhibited a lower charge transfer resistance (R_{ct}) in the high-frequency region (9.0 Ω) compared to RuO₂ (11.1 Ω), CoO_x (20.1 Ω), FeCrO_x (45.4 Ω), and NiCrO_x (21.6 Ω), suggesting superior electrical conductivity and expedited charge transfer process. Corroborating this trend, a comparative analysis of the electrochemically active surface area (ECSA) of the catalysts (Fig. 3e and Supplementary

Fig. 14) was undertaken, obtained by measuring the double-layer capacitance in the non-faradaic potential region. The C_{dl} for CoCrO_x was calculated to be 16.45 mF cm⁻², higher than FeCrO_x (6.13 mF cm⁻²), NiCrO_x (7.56 mF cm⁻²), CoO_x (12.12 mF cm⁻²) and RuO₂ (9.95 mF cm⁻²). Notably, both EIS and kinetic analyses are in accordance with the excellent activity of CoCrO_x observed in the LSV curves. Stability is also a key criterion to evaluate the long-term catalytic performance of electrocatalysts (Supplementary Fig. 15). CoCrO_x exhibited no significant loss of activity during 50 h of electrolysis in a half-cell at the constant voltage of 1.56 V (*vs* RHE), with the current density first increasing and then stabilizing. The increase in current density could be attributed to the formation of more active material and the gradual penetration of the electrolyte into the porous structure²³.

In order to capture the industrial potential of CoCrO_x electrocatalysts, we constructed an AEM electrolyzer system with the prepared samples as an anode catalyst and commercial Pt/C as a cathode catalyst to evaluate its catalytic performance under simulated industrial conditions (60 °C). The current-voltage (I-V) characteristic curves in Fig. 3f demonstrate that the CoCrO_x catalyst displays superior performances, achieving the high current density of 1.5 A cm⁻² at 2.1 V. We also investigated the impact of different membrane electrode

preparation methods on electrolyzer performance (Supplementary Fig. 16) and plotted the schematic diagrams of the electrolyzer assemblies for the three processes (Supplementary Fig. 17). To provide clarification for the outstanding performance of CoCrO_x catalysts in AEMWE, the Nyquist plots of the electrolyzer obtained through EIS reveal three different resistances in AEMWEs: ohmic resistance (OR), charge-transfer resistance (CTR) and mass transport resistance (MTR) (Fig. 3g). The intercepts in the high-frequency region represents OR, while the high- and low-frequency regions arcs indicate the CTR associated with electrochemical reactions and MTR corresponding to the transportation of reactants and products, respectively. It is evident that the OR of the samples are nearly identical, with CoCrO_x exhibiting the lowest CTR and MTR, indicating its superior activity derives from expedited charge transport and reduced mass transfer resistance. Supplementary Fig. 18 demonstrates that the *operando* EIS was employed at various currents to determine the charge transfer resistance of each catalyst. The obtained results indicated a notable decline in resistance with increased current, implying faster electron transfer and higher energy conversion efficiency during electrolysis at elevated currents. We additionally assessed the stability of the CoCrO_x catalyst under 60 °C and room temperature conditions at a high current density of 0.5 A cm^{-2} to further evaluate its potential for industrial applications (Fig. 3h and Supplementary Fig. 19). As shown in Fig. 3h, the catalyst displayed considerable stability during electrolysis durations of 120 h, verifying their practicability for real-world deployment. The diagram presented in Fig. 3h displays a diagrammatic representation of the AEMWE, which includes two stainless steel (SS) collectors with runners, two polytetrafluoroethylene (PTFE) gaskets, titanium felts, AEM, and carbon paper (CP). The various electrochemical data are compiled in Supplementary Table 2 for a cleaner comparison and contrast of each catalyst's electrochemical performance.

Valence and local structure evolution analysis

In order to compare and investigate the key reasons for the excellent activity of CoCrO_x , the initial valence state of the active elements in unison is determined. By X-ray near-edge structural absorption spectroscopy (XANES), we were able to precisely determine the valence states of the active elements. For transition metal elements, the rightward shift of the nearside absorption edge represents an elevated oxidation state. Comparing the position of the absorption edge to the standard samples reveals that CoCrO_x is located between CoO and Co_3O_4 (Fig. 4a). In addition, the leftward shift of the absorption edge of CoCrO_x relative to CoO_x indicates that the Cr doping decreases the average valence state of Co, which matches the stronger lower valence absorption peak in the soft XAS (sXAS) (Supplementary Fig. 20). The coexistence of both +2 and +3 valences for each active metal element in X-ray photoelectron spectroscopy (XPS) also confirms the above conclusion (Supplementary Fig. 21a–f and Supplementary Table 3). Correspondingly, the valence states of Cr-doped Fe and Ni (Supplementary Fig. 22) were similarly stabilized between +2 and +3 valence. Figure 4b shows that the Cr *K*-edge of all catalysts almost overlaps with Cr_2O_3 , pointing to the valence state of Cr is +3, which is in high agreement with the results in sXAS (Supplementary Fig. 23) and XPS (Supplementary Fig. 21g–i). The consistency between valence and structure bolsters the reliability of further analysis. To further elucidate the reason for the difference in the intrinsic catalytic activity of the three catalysts, we examined the valence alterations in the active elements of FeCrO_x , CoCrO_x and NiCrO_x before and after the reaction using sXAS (Fig. 4c and Supplementary Fig. 24). We discovered a conspicuous change in Co alone during the reaction, its absorption peak shifted by 1.9 eV towards the higher energy, representing a significant increase in the oxidation state of Co, which is also supported by the XPS results (Supplementary Fig. 25). Given that the binding energy of Co^{2+} is higher than that of Co^{3+} , the shift in the binding energy peak to the lower energy corroborates the higher valence

state^{24,25}. It is also evident that the characteristic satellite peak of Co^{2+} almost disappears, further proving that Co^{2+} is almost completely oxidized to the higher valence state during the OER process.

To further uncover the dynamic evolution of the electronic structure and atomic local environment of the Co active sites during the electrocatalytic OER, the in-situ XAFS and vtc-XES measurements were performed using a lab-built electrochemical cell. As shown in Fig. 4d, the Co *K*-edge XANES spectra indicate that the positions of the absorption edge of Co under ex-situ and open-circuit voltage (OCV) conditions are almost the same. When the voltage is applied, the near-edge absorption edge of Co is positively shifted, implying the elevation of the average oxidation state of Co during the OER process, which is consistent with the sXAS and XPS results. The fitted results of the Co *K*-edge EXAFS spectra indicate that the coordination number of the first shell layer (Co-O) increases significantly from 4 to above 6 as the voltage is applied (Fig. 4e, Supplementary Fig. 26 and Supplementary Table 4), and the increase in coordination number may be the reason for the elevated Co valence state^{26,27}. The graph depicted intuitively in Fig. 4f illustrates a significant positive correlation between the absorption edge position and the Co-O coordination number. In addition, we noted that the local structure of Co changed during the reaction, which may indicate the dynamic reconfiguration of CoCrO_x ^{28,29}. This is due to the partial electrolytic dissolution of Cr under alkaline conditions, which is supported by the reduction of Cr content revealed EDS mappings after reaction (Supplementary Fig. 27). The HRTEM results (Supplementary Fig. 28a) indicate that the catalyst essentially maintained its original morphology, but short lattice streaks and nanopores appeared, and these formed pores may provide a larger specific surface area and easy access to the active sites, as well as rapid mass transfer, which would further promote the OER kinetics^{30,31}. The amorphous structure may have been slightly damaged during the electrolysis process, as evidenced by several bright spots in the SAED pattern after reaction. However, the original amorphous state was largely preserved (Supplementary Fig. 28b).

Although EXAFS can provide the coordination numbers as well as the metal-ligand bond lengths, it fails to distinguish between ligands with similar atomic numbers (e.g., C, N, O) or different protonation states of the ligands³². Therefore, the in-situ vtc-XES (Fig. 4g) was employed to identify the ligand and coordination environment of Co, thereby further confirm the ligand type and the variation in bond strength. The $K\beta''$ peak around 7690 eV is significant evidence of ligand-metal interaction through σ interactions³³, and this peak is recognized as the characteristic peak of Co-O coordination³⁴. An intensified $K\beta''$ peak characterized implied that the Co-O interaction strengthens with voltage during the OER. This observation corroborates the contraction of the Co-O bond distance as depicted in the Fourier-transformed EXAFS (FT-EXAFS) spectra³⁵. The subtracted spectra vtc-XES is illustrated on the top of Fig. 4g to highlight the differences. It is observable that post-voltage application, the peak intensity closely resembles that of the Co_3O_4 reference sample ($R_{\text{Co-O}} = 1.92 \text{ \AA}$). Furthermore, Fig. 4h showcases the dependable negative connection between the intensity of the subtracted vtc-XES spectra and the Co-O bond lengths, thereby corroborating the reliability of the analysis. Shorter Co-O bonds can provide optimized binding energy for the adsorption of oxygen intermediate, thereby facilitates the accelerated OER kinetic process^{36,37}.

Mechanism investigation and simulation

In order to gain deeper understanding of the adsorption behaviors and reaction mechanisms of various catalysts, we conducted in-situ SR-IR measurements and density functional theory (DFT) calculations for FeCrO_x , CoCrO_x and NiCrO_x . As presented in Fig. 5a, the reflectance intensity heatmap obtained from SR-IR spectroscopy of CoCrO_x indicate the three crucial reactive intermediates of OER, namely *OH (3780 cm^{-1}), *OOH (1014 cm^{-1}) and *O (930 cm^{-1})^{38–41}. Interestingly, the *O adsorption peaks only appear at higher potentials. When the

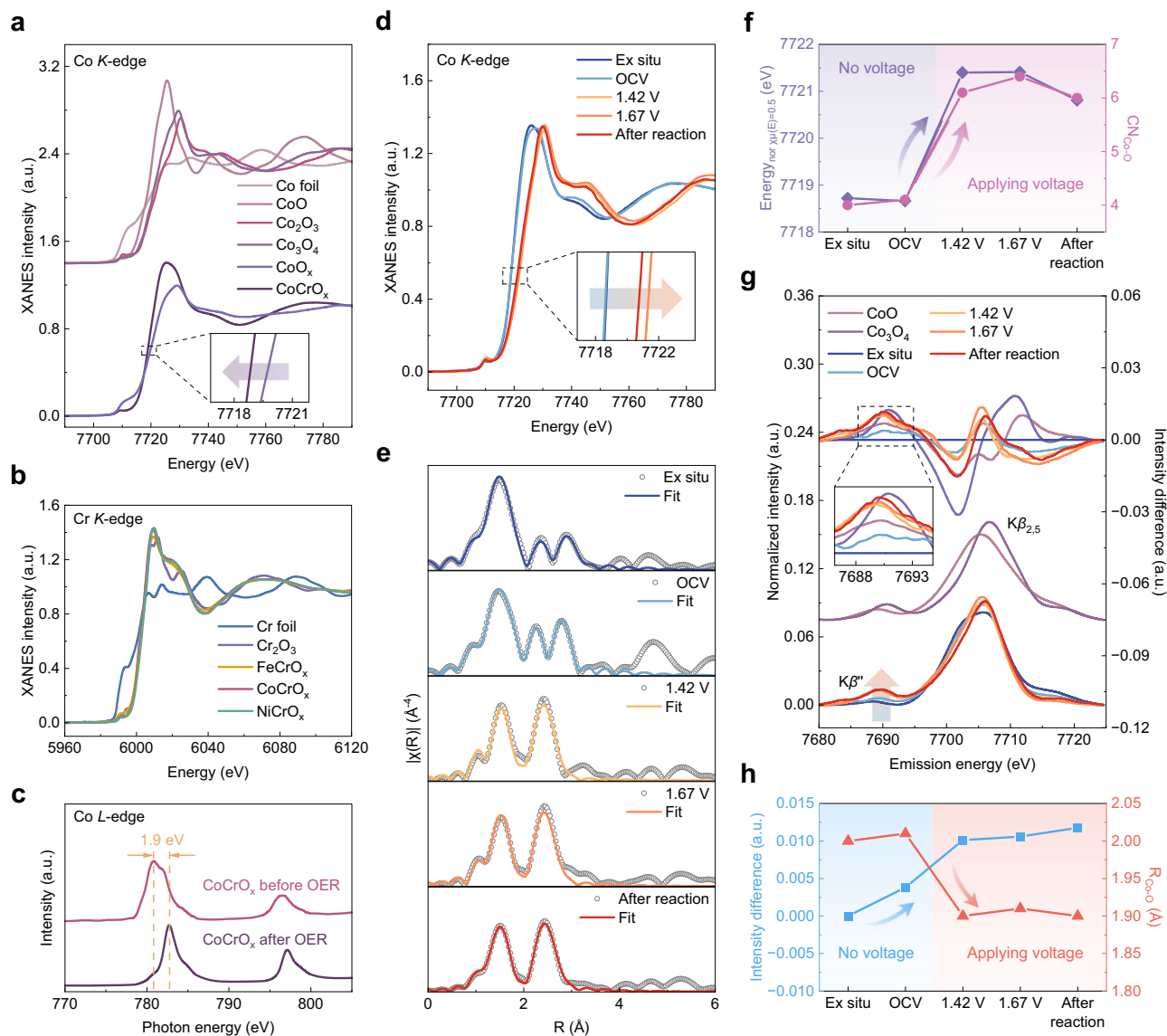


Fig. 4 | Valence state, change in catalyst properties recorded at different applied voltages during electrocatalytic OER. **a** XANES spectra of Co *K*-edge of CoO_x , CoCrO_x and the reference samples. **b** XANES spectra of Cr *K*-edge of FeCrO_x , CoCrO_x , NiCrO_x and the reference samples. **c** Normalized sXAS spectra of Co *L*-edge of CoCrO_x before and after OER. **d** In-situ XANES spectra of CoCrO_x . **e** The fitting curves of k^3 -weighted FT-EXAFS spectra of Co *K*-edge for CoCrO_x .

f Relationship between normalized absorption edge energy [$\chi\mu(E)=0.5$] and Co-O coordination number during the OER process. **g** In-situ vtc-XES spectra of CoCrO_x and the reference samples. The subtracted vtc-XES spectra (each spectrum minus ex-situ spectrum) is shown at the top highlight the differences. **h** Relationship between intensity differences in in-situ vtc-XES spectra and Co-O bond lengths during the OER process.

potential reaches the OER region (≥ 1.4 V), the intensities of the $^*\text{OH}$ and $^*\text{O}$ peaks markedly increase. This indicates a positive correlation between intermediate adsorption and voltage application. Nevertheless, the intensity of the $^*\text{OOH}$ peak paradoxically weakens or even vanishes (Fig. 5b and Supplementary Fig. 29b). In contrast, no $^*\text{O}$ adsorption peaks were observed for FeCrO_x and NiCrO_x at all potential conditions, suggesting that CoCrO_x has an optimized intermediate adsorption energy (Supplementary Fig. 29a, c). This finding further corroborates that $^*\text{O}$ is produced and adsorbed on the Co sites during the reaction of CoCrO_x , resulting in an increase in the number of Co-O ligands and the Co valence change, which in turn facilitates the OER process⁴¹.

To elucidate the rationale behind these occurrence, a four-electron OER mechanism was assumed to proceed through $^*\text{OH}$, $^*\text{O}$ and $^*\text{OOH}$ (asterisks denote adsorption sites) (Fig. 5c)⁴². The Gibbs free energy and the limiting reaction barrier were also calculated for each elementary step in the OER, which based on the free energy of the

rate-determining step (RDS) (Fig. 5d). It was discovered that for CoCrO_x , the RDS is the oxidation of $^*\text{OH}$ to $^*\text{O}$, which may be a plausible explanation for the fact that $^*\text{O}$ is generated only at higher potentials. Whereas the $^*\text{OOH}$ dehydrogenation to form O_2 exhibits the lowest reaction energy barrier in comparison to the other three steps. As a result, the $^*\text{OOH}$ intermediates are consumed rapidly at high potentials, potentially explaining the near disappearance of the $^*\text{OOH}$ peak. It is pertinent to mention that CoCrO_x exhibited the lowest RDS among three catalysts, measuring only 0.50 eV at $U=1.23$ V. The RDSs for the oxidation of $^*\text{O}$ to $^*\text{OOH}$ in FeCrO_x and NiCrO_x were 0.76 eV and 0.63 eV, respectively. Furthermore, the differential charge densities in Fig. 5e reveals that the charge transfer of CoCrO_x to $^*\text{OH}$ is significantly less and the interactions are weaker compared to FeCrO_x and NiCrO_x . This corresponds to the relatively weaker adsorption of $^*\text{OH}$ intermediates in the CoCrO_x free energy diagram. The optimized $^*\text{OH}$ adsorption allows the subsequent steps to occur at lower potentials, thus facilitating the OER kinetics⁴³. Meanwhile, the total density of

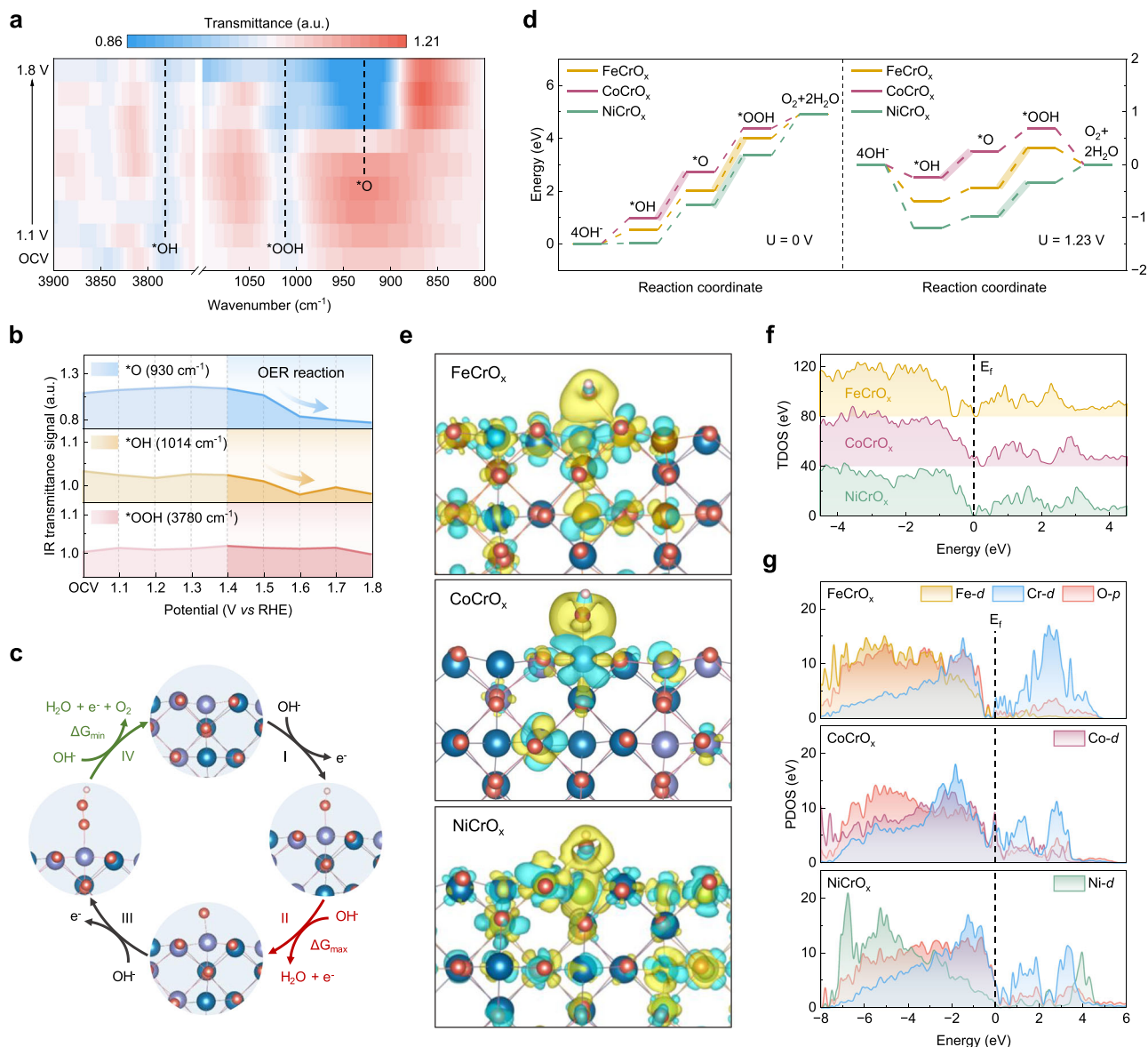


Fig. 5 | Monitoring of reaction intermediates and DFT calculations. **a** In-situ SR-IR measurements in the range of 3900–3750 cm^{-1} and 1100–800 cm^{-1} under various potentials for CoCrO_x , during the OER process. **b** Infrared transmittance signals versus potentials of $^*\text{O}$, $^*\text{OH}$ and $^*\text{OOH}$ intermediates. **c** The proposed alkaline OER mechanism on CoCrO_x . The model colors are Co (purple), Cr (blue), O (red) and H (pale pink). **d** OER free-energy diagrams at 0 V (left) and 1.23 V (right) for FeCrO_x , CoCrO_x and NiCrO_x . **e** Differential charge densities (blue and yellow regions indicate electron depletion and accumulation, respectively). The model colors are Fe (yellow-brown), Co (purple), Ni (green), Cr (blue), O (red) and H (pale pink). **f** TDOS and **(g)** PDOS of FeCrO_x , CoCrO_x and NiCrO_x .

states (TDOS) calculation shows that CoCrO_x has greater density of states at the Fermi energy level, suggesting improved conductivity and explaining the exceptional activity of CoCrO_x (Fig. 5f). The projected density of state (PDOS) illustrates that Fe/Co/Ni d - and O p -orbital electrons contributions are mainly in the valence band, whereas the conduction band is composed predominantly Cr d -orbital electrons (Fig. 5g). Further analysis of the d orbitals of the active metal reveals that the d_{xy} , d_{yz} , d_{z^2} , d_{xz} and $d_{x^2-y^2}$ orbital projections of Fe, Co, and Ni mainly contribute below the Fermi level and have strong orbital interactions with the O $2p$ orbitals, indicating that Fe/Co/Ni has stable bonding ability with O atoms, which is conducive to promoting adsorption of active O atoms and OER kinetics (Supplementary Figs. 30, 31). In addition, the electron density near the Fermi energy level of the active elements is primarily contributed by the $d_{x^2-y^2}$ orbitals. However, the abundance of d electrons near the Fermi level, rather than significantly below it, facilitates the charge transfer from

transition metals to oxygen-containing adsorbates during the OER process⁴⁴. This is particularly evident in the case of CoCrO_x , which is significantly higher than FeCrO_x and NiCrO_x . This further corroborates the reason for its exceptional activity.

Discussion

To summarize, we elaborated and synthesized a series of high-valent Cr-doped amorphous metal oxide catalysts using a facile one-step liquid phase reduction method. The CoCrO_x catalyst achieved a high current density of 1.5 A cm^{-2} at 2.1 V and operated at a current density of 0.5 A cm^{-2} for over 120 h in the AEMWE. In-situ synchrotron measurements and theoretical calculations indicate that optimized $^*\text{O}$ adsorption, shorter Co-O bond lengths, and elevated coordination numbers resulted in Co valence changes and improved OER activity. Hence, the low oxidation energy barrier of the active metal is the ultimate goal of electronic structure modulation, which is the key

factor for the greater activity of the easily oxidized transition metals. These findings broaden the pathway to enhance OER catalytic activity and practical AEMWEs performance, while the application of new in-situ method suggests numerous possibilities for addressing relevant problems in the field of energy catalytic reactions.

Methods

Chemicals

Iron chloride hexahydrate ($\text{FeCl}_3 \cdot 6\text{H}_2\text{O}$), nickel chloride hexahydrate ($\text{NiCl}_2 \cdot 6\text{H}_2\text{O}$), cobalt chloride hexahydrate ($\text{CoCl}_2 \cdot 6\text{H}_2\text{O}$), chromium chloride hexahydrate ($\text{CrCl}_3 \cdot 6\text{H}_2\text{O}$), sodium borohydride (NaBH_4) and ethanol were purchased from Sinopharm Chemical Reagent Co., Ltd. Potassium hydroxide (KOH, electronic grade, 99.999% metals basis, except sodium) was purchased from Shanghai Aladdin Biochemical Technology Co., Ltd. Ruthenium dioxide (99.9% trace metals basis) and Nafion[®]117 solution (5%) were purchased from Sigma-Aldrich. Carbon black (ECP600JD, Ketjenblack[®]) for electrochemical measurements was obtained from Suzhou Sinero Technology Co., Ltd. and graphite powder (XF009 7782-42-5) for XAS characterization was obtained from XFNANO Materials Tech Co., Ltd. All chemicals can be used without further purification.

Synthesis of catalysts

Dissolve 11.90 g of $\text{CoCl}_2 \cdot 6\text{H}_2\text{O}$ and 13.32 g of $\text{CrCl}_3 \cdot 6\text{H}_2\text{O}$ in 25 mL of deionized (DI) water to make a 2 M metal chloride solution and set aside. Take 2 mL of the above prepared CoCl_2 and CrCl_3 solutions respectively and mix them evenly. Prepare a fresh solution of sodium borohydride by dissolving 3 g of NaBH_4 in 20 mL of DI water, then add dropwise to the above mixture of metal ion chlorides, stir mechanically for 15 min, allow to cool, then leave overnight and freeze dry. After freeze-drying, the catalyst was repeatedly washed using DI water and ethanol, and dried under vacuum to obtain the CoCrO_x catalyst. FeCrO_x , NiCrO_x and CoO_x catalysts were obtained by the same procedure, except that the metal chloride solution was replaced with another.

Electrochemical measurements

All electrochemical tests were performed in a typical three-electrode system on an electrochemical workstation (CHI760E, Chen Hua). A Hg/HgO electrode (1 M KOH, Tjaida) was used as the reference electrode, a platinum foil electrode ($10 \times 15 \times 0.3$) or graphite rod as the counter electrode and the catalyst was coated on 0.5×0.5 cm carbon paper (HESEN, HCP020N) to make a working electrode. 6 mg of catalyst, 3 mg of conductive carbon black (ECP600JD, Ketjenblack[®]) was homogeneously mixed with 475 μL of DI water, 475 μL of ethanol and 50 μL of 5 wt% Nafion and sonicated to make a homogeneous ink. 495 μL of DI water, 495 μL of ethanol and 10 μL of 5 wt% Nafion were mixed to make 0.05 wt% Nafion solution. Then 15 μL of catalyst ink was dropped onto carbon paper (0.36 mg cm^{-2}), dried and 7.5 μL of 0.05 wt% Nafion was added dropwise and dried at room temperature and used for electrochemical measurements.

Linear scanning voltammetry (LSV) was performed in oxygen-saturated 1 M KOH at room temperature (25 °C) using a scan rate of 5 mV/s. The solution resistance R_s was determined from the resulting Nyquist plot fit and used for ohmic drop correction based on $E_c = E_m - iR_s$ where E_c is the correction potential and E_m is the measured potential, respectively). EIS spectra were measured over a range of 0.1–100 kHz with an amplitude of 0.005 V. The voltage was set at 1.57 V (νs RHE) and the EIS data was fitted by ZView software. In the equivalent circuit diagram (inset of Fig. 3d), R_s represents the solution resistance, R_p and R_{ct} are the resistances for charge transfer, and C_l and C_{dl} are used to describe the double-layer capacitance. Electrochemical active surface area (ECSA) was obtained by measuring the double-layer capacitance in the nonfaradaic potential region with a voltage measurement range of 0.875 to 0.975 V (νs RHE).

MEAs fabrication and AEMWEs evaluation

The MEAs fabrication and AEMWEs evaluation were performed at Zhongke Enthalpy (Anhui) New Energy Technology Co, Ltd. For the anode, the prepared catalysts (FeCrO_x , CoO_x , CoCrO_x and NiCrO_x) catalysts were mixed with the ionomer (PiperION-A5-HCO3) in an aqueous solution (1:3 water and isopropanol). For the cathode, Pt/C (TANAKA, 40 wt%) was mixed with the ionomer in an aqueous solution (1:5 water and isopropanol). The catalyst ink was sprayed onto AEM (PiperION-A60-HCO3) or platinum-titanium-coated felt (Sti0.25Pt0.5) to make gas diffusion electrodes (GDEs), with an approximate metal loading of 1 mg cm^{-2} for the anode and 1.5 mgPt cm^{-2} for the cathode. The AEM was immersed in 0.5 M KOH for 1 h, then replaced with fresh KOH solution and immersed for another 1 h. The bicarbonate anion was then rinsed with deionized water to convert the bicarbonate anion to hydroxide anion. The MEA was loaded into a fixture and clamped with a torque of 8 N·m. The cell was tested by a constant-potentiostat with a flowing electrolyte of 1 M KOH, and the AEMWEs were tested for internal resistance using an internal resistance meter (20 m Ω for FeCrO_x , 15 m Ω for CoO_x , 24 m Ω for CoCrO_x and 22 m Ω for NiCrO_x). The ohmic drop was calculated based on the $E_c = E_m - iR_s$ correction for iR compensation. EIS measurements of the AEMWEs were performed by an impedance analyzer (DH7007, DongHua Analytical) over the range of 0.1–10k Hz, amplitudes of 50–250 mA, and currents of 0.5–2.5 A (The applied RMS AC is 10% of the corresponding DC and the effective area of the MEA is 5 cm²). The performance and EIS tests were conducted at a temperature of 60 °C, while the durability tests were conducted at both 60 °C and room temperature.

Material characterizations

XRD patterns were obtained by using a Philips X'Pert ProSuper diffractometer with Cu K α radiation ($\lambda = 1.54178 \text{ \AA}$). The morphology was examined by SEM using the ZEISS GeminiSEM 500. TEM and HRTEM images were undertaken on a JEM-2100F field-emission electron microscope with an accelerating voltage of 200 kV. HAADF-STEM was performed on a JEOL JEM-ARF200F HRTEM with a spherical aberration corrector at voltage of 200 kV. EDS elemental mappings were obtained on JEOL JEM-F200 instrument. All catalysts for synthesis were dissolved in aqua regia and obtain the contents of Fe, Co, Ni and Cr in as-prepared catalysts were determined by ICP-AES on a PerkinElmer Optima 7300 DV ICP-AES instrument. The XPS were recorded on a Thermo ESCALAB 250Xi spectrometer with an excitation source of monochromatized Al K α ($h\nu = 1486.6 \text{ eV}$) and a pass energy of 30 eV. The values of binding energies were calibrated with the C 1s peak of contaminant carbon at 284.80 eV.

Soft X-ray XANES measurements

The L-edge XANES measurements of Fe, Co, Ni and Cr were performed at the photoemission endstation at BL12B beamlines of the National Synchrotron Radiation Laboratory (NSRL), China. A bending magnet was connected to the beamline, which was equipped with three gratings covering photon energies from 100 to 1000 eV with an energy resolution of $\sim 0.2 \text{ eV}$. The data were recorded in the total electron yield mode by collecting the sample drain current. The resolving power of the grating was typically $E/\Delta E = 2000$, and the photon flux was 1×10^9 photons per second.

XAFS measurements

The XAFS spectra were measured at the BL14W1 beamline of the Shanghai Synchrotron Radiation Facility (SSRF) and the 1W1B beamline of the Beijing Synchrotron Radiation Facility (BSRF), China. The SSRF storage ring was operated at 3.5 GeV and the BSRF at 2.5 GeV, both with a maximum electron current of 250 mA. A total of about 64 mg of the appropriate sample was homogeneously mixed with graphite and pressed into round pellets of 8 mm diameter. The spectra of the K-edge of Cr (5989 eV), Fe (7112 eV), Co (7709 eV) and Ni (8333 eV) for

all samples were recorded in transmission mode, and the position of the absorption edge (E_0) was calibrated by the corresponding element foil, respectively.

The in-situ XAFS spectra were measured at the BL14W1 beamline of the SSRF, China. The in-situ XAFS measurements were performed with catalyst-coated carbon paper using a home-built electrolytic cell, the spectra of which were collected in fluorescent mode. The catalyst powders were homogeneously dispersed in water and ethanol ($v:v = 1:1$) to form an ink, which was dropcast onto the carbon paper as a working electrode. To obtain the evolution information of the Co sites under OER working conditions, XAFS spectra were analyzed for a series of presentative conditions (ex situ, OCV, 1.42 V vs RHE and 1.67 V vs RHE, after reaction).

XAFS data analysis

The acquired EXAFS data were processed according to standard procedures using the ATHENA module implemented in the IFEFFIT software package⁴⁵. The k^3 -weighted $\chi(k)$ data in the k -space were Fourier-transformed into real (R) space using a hanning windows ($dk = 1.0 \text{ \AA}^{-1}$) to separate the EXAFS contributions from different coordination shells. To obtain detailed structural parameters around the Co atoms in the as-prepared samples, quantitative curve fitting was performed on for the Fourier-transformed $k^3\chi(k)$ in R-space using the ARTEMIS module of IFEFFIT⁴⁶. The effective backscattering amplitude $F(k)$ and the phase shift $\Phi(k)$ of all fitting paths were calculated using the ab initio code FEFF8.0⁴⁷. For different in-situ samples, the k range of $[3.0, 10.8] \text{ \AA}^{-1}$ and the R range of $[1.0, 3.2] \text{ \AA}$ were used for ex-situ and OCV samples. For 1.42 V vs RHE, 1.67 V vs RHE and after reaction samples, the k range of $[3.0, 11.5] \text{ \AA}^{-1}$ and the R range of $[1.0, 3.0] \text{ \AA}$ were chosen. For the selected R range for k^3 -weighted $\chi(k)$ for the curve fitting function, the number of independent points is given by

$$N_{ipt} = \frac{2\Delta k \times \Delta R}{\pi} \quad (1)$$

As for ex-situ and OCV samples:

$$N_{ipt1} = \frac{2 \times (10.8 - 3) \times (3.2 - 1)}{\pi} = 10.9 \quad (2)$$

For 1.42 V, 1.67 V and after reaction samples:

$$N_{ipt2} = \frac{2 \times (11.5 - 3) \times (3.0 - 1)}{\pi} = 10.8 \quad (3)$$

During the curve fitting, the amplitude-efficient reduction factor (S_0) was fixed at the value of 0.71 for Co samples determined by fitting the data of Co foil, with the coordination number of Co-Co set to 12.

For the ex-situ and OCV samples, the FT curves showed three peaks near 1.5 Å, 2.3 Å and 2.8 Å, which were assigned to Co-O, Co-Co and Co-Cr coordination, respectively. Subsequently, a three-shell structure model including a Co-O, a Co-Co and a Co-Cr scattering path was used to fit the EXAFS data of the in-situ samples. In both samples, the Debye-Waller factors (σ^2) set to be the same, the σ^2 of the first shell layer (Co-O) of the OCV sample was set as a free parameter. Meanwhile, the σ^2 of the ex-situ sample was set to the best fitting value for the OCV sample. The coordination numbers (CN), interatomic distances (R), and energy shifts (ΔE_0) were all set as free parameters for both samples.

Therefore, the number of adjustable parameters for the ex-situ sample is

$$N_{para1} = 3 + 3 + 3 = 9 < N_{ipt1} = 10.9 \quad (4)$$

For the OCV sample, the number of adjustable parameters is

$$N_{para2} = 4 + 3 + 3 = 10 < N_{ipt1} = 10.9 \quad (5)$$

For the 1.42 V, 1.67 V and after reaction samples, the FT curves showed two peaks near 1.5 Å and 2.4 Å assigned to Co-O and Co-Co coordination, which were fitted using a two-shell structure model including one Co-O and one Co-Co scattering path. Considering these three samples, σ^2 should be set to be consistent and CN, R and ΔE_0 were set as free parameters.

Hence, the number of adjustable parameters for the three samples is

$$N_{para3} = 3 + 3 = 6 < N_{ipt2} = 10.8 \quad (6)$$

All yielded R-factors for all samples were no larger than 0.020, indicating the appropriate modeling, rational parameter settings and thus, the good fitting qualities.

Vtc-XES measurements

The Co vtc-XES measurements were measured at the BL20U beamline (E-line) of SSRF, China. The incident X-ray was monochromatized to 7706 eV by Si (111) double-crystal monochromator. Five Si (440) spherical crystals and a Pilatus3 photon counting detector were used to collect and analysis Co $K\beta_{2,5}$ and $K\beta''$ fluorescence more efficiently. To reduce the absorption of fluorescence by air, a helium gas bag was placed between the sample, spherical crystals, and the detector. The in-situ setup was identical to the in-situ XAFS measurements. The vtc-XES spectra were baseline-corrected using a straight line and normalized to the total area between 7624.6 and 7680 eV, and then the data were smoothed using the Savitzky-Golay method.

In-situ SR-IR measurements

In-situ SR-IR measurements were conducted at the infrared beamline BLOIB of NSRL using a homemade top-plate cell reflection IR setup with a ZnSe crystal as the infrared transmission window. The catalyst electrode was pressed tightly against the ZnSe crystal window with a micron-scale gap to minimize the loss of infrared light. To ensure high-quality SR-IR spectra, the apparatus utilized a reflection mode with a vertical incidence of infrared light. The infrared spectrum was obtained by averaging 128 scans at a resolution of 4 cm^{-1} . Prior to each systemic OER measurement, the background spectrum of the catalyst electrode was obtained at an open-circuit voltage. The OER potential ranges were measured between 1.1–1.8 V vs RHE with an interval of 0.1 V. The infrared data was processed and smoothed using OPUS software.

DFT calculations

The calculations were performed within the Density Functional Theory (DFT) framework implanted in Vienna ab initio Simulation Package (VASP)⁴⁸. The interaction between ions and electrons was described in the Projector Augmented Wave (PAW) Method⁴⁹. The electron exchange and correlation energy were described using the generalized gradient approximation-based Perdew–Burke–Erzenhorf (PBE) functional⁵⁰. The semi-empirical London dispersion corrections of Grimme and colleagues (DFT-D3) were conducted to calculate the interactions between absorbers and slabs⁵¹. The Hubbard-U correction was applied for better description of the localized d-electrons of Fe, Co and Ni. We chose an effective U–J value of 3.0 eV for Fe, 3.5 eV for Co and 5.5 eV for Ni atoms^{52,53}. The surface structure models of FeCrO_x (110), CoCrO_x (110) and NiCrO_x (110) were built. A sufficiently large vacuum region of 15 Å was used for all the models to ensure the periodic images were well separated. The Brillouin-zone integrations were carried out using Monkhorst-Pack grids of special points. A gamma-centered ($4 \times 3 \times 1$) k-point grid were used for supercell. To obtain the accurate structure, the plane-wave cutoff energy was set up to 500 eV.

The force convergence was set to be $<0.02 \text{ eV } \text{Å}^{-1}$, and the total energy convergence was set to be $<10^{-5} \text{ eV}$. The free energy of the adsorbed state was calculated as follows based on the adsorption energy:

$$\Delta G^{\ddagger} = \Delta E^{\ddagger} + \Delta E_{\text{ZPE}} + U_{(\text{T})} - T\Delta S \quad (7)$$

where ΔE^{\ddagger} is the adsorption energy directly obtained from DFT calculations, ΔE_{ZPE} is the zero-point energy, $U_{(\text{T})}$ is the heat capacity correction energy, and T is the temperature ($T = 298.15 \text{ K}$), ΔS is the change in entropy. Herein, the Gibbs energy is corrected by using the VASPkit code⁵⁴.

Data availability

The source data underlying Figs. 2–5, Supplementary Figs. 3, 9–16, 18–26, 29–31 and the electronic structure calculations generated in this study are provided as a Source Data file. Source data are provided with this paper.

References

- Abbasi, R. et al. A roadmap to low-cost hydrogen with hydroxide exchange membrane electrolyzers. *Adv. Mater* **31**, 1805876 (2019).
- Xu, D. et al. Earth-abundant oxygen electrocatalysts for alkaline anion-exchange-membrane water electrolysis: effects of catalyst conductivity and comparison with performance in three-electrode cells. *ACS Catal* **9**, 7–15 (2018).
- Li, D. et al. Highly quaternized polystyrene ionomers for high performance anion exchange membrane water electrolyzers. *Nat. Energy* **5**, 378–385 (2020).
- Seh, Z. W. et al. Combining theory and experiment in electrocatalysis: insights into materials design. *Science* **355**, eaad4998 (2017).
- Li, Q. et al. Anion exchange membrane water electrolysis: the future of green hydrogen. *J. Phys. Chem. C* **127**, 7901–7912 (2023).
- Cousins, I. T. et al. The concept of essential use for determining when uses of PFASs can be phased out. *Environ. Sci. Processes Impacts* **21**, 1803–1815 (2019).
- Santoro, C. et al. What is next in anion-exchange membrane water electrolyzers? Bottlenecks, benefits, and future. *ChemSusChem* **15**, e202200027 (2022).
- Li, C. & Baek, J.-B. The promise of hydrogen production from alkaline anion exchange membrane electrolyzers. *Nano Energy* **87**, 106162 (2021).
- Xu, H. et al. Carbon-based bifunctional electrocatalysts for oxygen reduction and oxygen evolution reactions: optimization strategies and mechanistic analysis. *J. Energy Chem.* **71**, 234–265 (2022).
- Wu, Q. et al. Non-covalent ligand-oxide interaction promotes oxygen evolution. *Nat. Commun.* **14**, 997 (2023).
- Yao, N. et al. Intermolecular energy gap-induced formation of high-valent cobalt species in CoOOH surface layer on cobalt sulfides for efficient water oxidation. *Angew Chem. Int. Ed.* **61**, e202117178 (2022).
- Zheng, X. et al. Theory-driven design of high-valence metal sites for water oxidation confirmed using in situ soft X-ray absorption. *Nat. Chem.* **10**, 149–154 (2018).
- Zhang, B. et al. High-valence metals improve oxygen evolution reaction performance by modulating 3d metal oxidation cycle energetics. *Nat. Catal* **3**, 985–992 (2020).
- Li, N. et al. Influence of iron doping on tetravalent nickel content in catalytic oxygen evolving films. *Proc. Natl Acad. Sci. USA* **114**, 1486–1491 (2017).
- Xiao, Z. et al. Operando identification of the dynamic behavior of oxygen vacancy-rich Co_3O_4 for oxygen evolution reaction. *J. Am. Chem. Soc.* **142**, 12087–12095 (2020).
- Novák, M. et al. Primary oxide minerals in the system $\text{WO}_3\text{-Nb}_2\text{O}_5\text{-TiO}_2\text{-Fe}_2\text{O}_3\text{-FeO}$ and their breakdown products from the pegmatite No. 3 at Dolní Bory-Hatě, Czech Republic. *Eur. J. Mineral* **20**, 487–499 (2008).
- Kuepper, K. et al. Electronic and magnetic properties of highly ordered $\text{Sr}_2\text{FeMoO}_6$. *Phys. Status Solidi A* **201**, 3252–3256 (2004).
- Wang, M. H. et al. Operando high-valence Cr-modified NiFe hydroxides for water oxidation. *Small* **18**, e2200303 (2022).
- Krishna, K. S., Sandeep, C. S. S., Philip, R. & Eswaramoorthy, M. Mixing does the magic: a rapid synthesis of high surface area noble metal nanospheres showing broadband nonlinear optical response. *ACS Nano* **4**, 2681–2688 (2010).
- Kim, J. J., Choi, Y., Suresh, S. & Argon, A. S. Nanocrystallization during nanoindentation of a bulk amorphous metal alloy at room temperature. *Science* **295**, 654–657 (2002).
- Wu, G. et al. A general synthesis approach for amorphous noble metal nanosheets. *Nat. Commun.* **10**, 4855 (2019).
- Cai, W. et al. Amorphous versus crystalline in water oxidation catalysis: a case study of NiFe alloy. *Nano Lett.* **20**, 4278–4285 (2020).
- Liu, J., Yang, Y., Ni, B., Li, H. & Wang, X. Fullerene-like Nickel Oxysulfide hollow nanospheres as bifunctional electrocatalysts for water splitting. *Small* **13**, 1602637 (2017).
- Zhang, R. et al. Synthesis and conductivity properties of $\text{Gd}_{0.8}\text{Ca}_{0.2}\text{BaCo}_2\text{O}_{5+\delta}$ double perovskite by sol-gel combustion. *J. Mater. Sci.: Mater. Electron.* **26**, 9941–9948 (2015).
- Qin, C. et al. Increasing cerium dispersion favours lattice oxygen activity of cobalt oxides for CO catalytic combustion. *Combust Flame* **260**, 113219 (2024).
- Wang, J. et al. Redirecting dynamic surface restructuring of a layered transition metal oxide catalyst for superior water oxidation. *Nat. Catal* **4**, 212–222 (2021).
- Zhou, J. et al. Electrochemically accessing ultrathin Co (oxy)-hydroxide nanosheets and operando identifying their active phase for the oxygen evolution reaction. *Energy Environ. Sci.* **12**, 739–746 (2019).
- Lv, L. et al. Coordinating the edge defects of bismuth with sulfur for enhanced CO_2 electroreduction to formate. *Angew Chem. Int. Ed.* **62**, e202303117 (2023).
- Zhu, J. et al. Surface passivation for highly active, selective, stable, and scalable CO_2 electroreduction. *Nat. Commun.* **14**, 4670 (2023).
- Xu, D. et al. The role of Cr doping in Ni Fe oxide/(oxy)hydroxide electrocatalysts for oxygen evolution. *Electrochim Acta* **265**, 10–18 (2018).
- Bo, X., Li, Y., Hocking, R. K. & Zhao, C. NiFeCr hydroxide holey nanosheet as advanced electrocatalyst for water oxidation. *ACS Appl. Mater. Interfaces* **9**, 41239–41245 (2017).
- Gallo, E. & Glatzel, P. Valence to core X-ray emission spectroscopy. *Adv. Mater* **26**, 7730–7746 (2014).
- Pollock, C. J. & DeBeer, S. Valence-to-Core X-ray emission spectroscopy: a sensitive probe of the nature of a bound ligand. *J. Am. Chem. Soc.* **133**, 5594–5601 (2011).
- Kuhn, T. J., Hormes, J., Matoussevitch, N., Bonnemann, H. & Glatzel, P. Site-selective high-resolution X-ray absorption spectroscopy and high-resolution X-ray emission spectroscopy of cobalt nanoparticles. *Inorg Chem.* **53**, 8367–8375 (2014).
- Pollock, C. J. & DeBeer, S. Insights into the geometric and electronic structure of transition metal centers from valence-to-core X-ray emission spectroscopy. *Acc. Chem. Res.* **48**, 2967–2975 (2015).
- Zhang, S. et al. Spontaneous delithiation under operando condition triggers formation of an amorphous active layer in spinel cobalt oxides electrocatalyst toward oxygen evolution. *ACS Catal* **9**, 7389–7397 (2019).
- Haase, F. T. et al. Size effects and active state formation of cobalt oxide nanoparticles during the oxygen evolution reaction. *Nat. Energy* **7**, 765–773 (2022).
- Su, H. et al. Dynamic evolution of solid-liquid electrochemical interfaces over single-atom active sites. *J. Am. Chem. Soc.* **142**, 12306–12313 (2020).

39. Su, H. et al. In-situ spectroscopic observation of dynamic-coupling oxygen on atomically dispersed iridium electrocatalyst for acidic water oxidation. *Nat. Commun.* **12**, 6118 (2021).
40. Lin, C. et al. In-situ reconstructed Ru atom array on α -MnO₂ with enhanced performance for acidic water oxidation. *Nat. Catal.* **4**, 1012–1023 (2021).
41. Zhou, Z. et al. Cation-vacancy-enriched Nickel phosphide for efficient electrosynthesis of hydrogen peroxides. *Adv. Mater.* **34**, 2106541 (2022).
42. Ullman, A. M., Brodsky, C. N., Li, N., Zheng, S. L. & Nocera, D. G. Probing edge site reactivity of oxidic cobalt water oxidation catalysts. *J. Am. Chem. Soc.* **138**, 4229–4236 (2016).
43. Zhang, L. et al. Fe-doped and sulfur-enriched Ni₃S₂ nanowires with enhanced reaction kinetics for boosting water oxidation. *Green Chem. Eng.* **3**, 367–373 (2022).
44. Zhao, C. et al. D-Orbital manipulated Ru nanoclusters for high-efficiency overall water splitting at industrial-level current densities. *Adv. Funct. Mater.* **34**, 2307917 (2024).
45. Newville, M. IFEFFIT: interactive XAFS analysis and FEFF fitting. *J. Synchrotron. Radiat.* **8**, 322–324 (2001).
46. Ravel, B. & Newville, M. ATHENA, ARTEMIS, HEPHAESTUS: data analysis for X-ray absorption spectroscopy using IFEFFIT. *J. Synchrotron. Radiat.* **12**, 537–541 (2005).
47. Ankudinov, A. L., Ravel, B., Rehr, J. J. & Conradson, S. D. Real-space multiple-scattering calculation and interpretation of x-ray-absorption near-edge structure. *Phys. Rev. B* **58**, 7565–7576 (1998).
48. Kresse, G. & J.F. Efficiency of ab-initio total energy calculations for metals and semiconductors using a plane-wave basis set. *Phys. Rev. B* **54**, 11169–11186 (1996).
49. Blöchl, P. E. Projector augmented-wave method. *Phys. Rev. B* **50**, 17953–17979 (1994).
50. Perdew, John P., Burke, Kieron & Ernzerhof, M. Generalized gradient approximation made simple. *Phys. Rev. Lett.* **77**, 3865–3868 (1996).
51. Grimme, S. Semiempirical GGA-type density functional constructed with a long-range dispersion correction. *J. Comput. Chem.* **21**, 1787–1799 (2006).
52. Conesa, J. C. Electronic structure of the (Undoped and Fe-Doped) NiOOH O₂ evolution electrocatalyst. *J. Phys. Chem. C* **120**, 18999–19010 (2016).
53. Tkalych, A. J., Zhuang, H. L. & Carter, E. A. A density functional + U assessment of oxygen evolution reaction mechanisms on β -NiOOH. *ACS Catal.* **7**, 5329–5339 (2017).
54. Wang, V., Xu, N., Liu, J.-C., Tang, G. & Geng, W.-T. VASPKIT: a user-friendly interface facilitating high-throughput computing and analysis using VASP code. *Comput. Phys. Commun.* **267**, 108033 (2021).
- (WK2060000038, WK2310000113), the Youth Innovation Promotion Association CAS (2022458). We would thank NSRL, BSRF and SSRF for the synchrotron beam time and the supercomputing system in the Supercomputing Center of University of Science and Technology of China for the calculations. This work was partially carried out at the Instruments Center for Physical Science, University of Science and Technology of China.

Author contributions

T.Y. conceived the idea and supervised the work. S.L., W.Z. and T.D. planned and performed the catalyst synthesis. S.L., M.W. and W.Z. performed the AEMWEs measurement. T.L., C.Q. and Q.L. carried out the DFT calculations. H.Z. and X.L. performed the XAFS measurements and assisted in analyzing the data. D.L., L.Z., Y.C., S.J., C.Q. and H.W. performed TEM, HRTEM, EDS-mapping measurements, and assisted in data analysis. T.Y., S.L., W.Z. and T.D. co-wrote, optimized and revised the manuscript. All authors discussed the results and provided comments on the manuscript.

Competing interests

The authors declare no competing interests.

Additional information

Supplementary information The online version contains supplementary material available at <https://doi.org/10.1038/s41467-024-47736-0>.

Correspondence and requests for materials should be addressed to Wei Zhang, Tao Ding or Tao Yao.

Peer review information *Nature Communications* thanks Jungang Hou and the other, anonymous, reviewers for their contribution to the peer review of this work. A peer review file is available.

Reprints and permissions information is available at <http://www.nature.com/reprints>

Publisher's note Springer Nature remains neutral with regard to jurisdictional claims in published maps and institutional affiliations.

Open Access This article is licensed under a Creative Commons Attribution 4.0 International License, which permits use, sharing, adaptation, distribution and reproduction in any medium or format, as long as you give appropriate credit to the original author(s) and the source, provide a link to the Creative Commons licence, and indicate if changes were made. The images or other third party material in this article are included in the article's Creative Commons licence, unless indicated otherwise in a credit line to the material. If material is not included in the article's Creative Commons licence and your intended use is not permitted by statutory regulation or exceeds the permitted use, you will need to obtain permission directly from the copyright holder. To view a copy of this licence, visit <http://creativecommons.org/licenses/by/4.0/>.

© The Author(s) 2024

Acknowledgements

This work was supported by the National Key R&D Program of China (2021YFA1600800), the National Natural Science Foundation of China (12025505, 22179125, and 12205304), the Guangdong Basic and Applied Basic Research Foundation (2022A1515011828), the Strategic Priority Research Program of the Chinese Academy of Sciences (XDB0450200), the University of China Innovation Program of Anhui Province (GXXT-2020-053), the Fundamental Research Funds for the Central Universities